NASA-TM-112480

Mechanisms of High-Temperature Fatigue Failure in Alloy 800H

K. BHANU SANKARA RAO, H. SCHUSTER, and G.R. HALFORD

The damage mechanisms influencing the axial strain-controlled low-cycle fatigue (LCF) behavior of alloy 800H at 850 °C have been evaluated under conditions of equal tension/compression ramp rates (fast-fast (F-F): 4×10^{-3} s^{-1} and slow-slow (S-S): 4×10^{-5} s^{-1}) and asymmetrical ramp rates (fast-slow (F-S): 4×10^{-3} s^{-1} / 4×10^{-5} s^{-1} and slow-fast (S-F): 4×10^{-5} / 4×10^{-3} s^{-1}) in tension and compression. The fatigue life, cyclic stress response, and fracture modes were significantly influenced by the waveform shape. The fatigue lives displayed by different loading conditions were in the following order: F-F > S-S > F-S > S-F. The fracture mode was dictated by the ramp rate adopted in the tensile direction. The fast ramp rate in the tensile direction led to the occurrence of transgranular crack initiation and propagation, whereas the slow ramp rate caused intergranular initiation and propagation. The time-dependent processes and their synergistic interactions, which were at the basis of observed changes in cyclic stress response and fatigue life, were identified. Oxidation, creep damage, dynamic strain aging, massive carbide precipitation, time-dependent creep deformation, and deformation ratcheting were among the several factors influencing cyclic life. Irrespective of the loading condition, the largest effect on life was exerted by oxidation processes. Deformation ratcheting had its greatest influence on life under asymmetrical loading conditions. Creep damage accumulated the greatest amount during the slow tensile ramp under S-F conditions.

I. INTRODUCTION

FULLY austenitic, iron-based, INCOLOY* 800H is

*INCOLOY is a trademark of INCO Alloys International, Inc., Huntington, WV.

used as a structural material in the petrochemical industry and for heat exchanger components in various energy conversion systems. In these applications, the components are often subjected to repeated thermal stresses as a result of temperature gradients which occur on heating and cooling during start-up and shut-down operations. Therefore, resistance to low-cycle fatigue (LCF) is an essential requirement. As a result, specific attention has been directed to the behavior of alloy 800H in recent years.[1–12] These investigations were conducted with the following objectives: (1) to ascertain the phenomenological effects of strain rate, strain range, and temperature on cyclic stress response and life under balanced cycling conditions;[1,2] (2) to evaluate environmental effects on LCF behavior;[3,4] (3) to assess the creep-fatigue interaction behavior by suitably designing and performing strain hold and asymmetrical slow-fast cycling tests;[5–8] (4) to evaluate the effects of hold time and frequency on crack growth and to arrive at suitable parameters for describing the crack growth behavior under pure fatigue

and creep-fatigue interaction;[9,10] (5) to determine the deformation and damage mechanisms under pure fatigue[1,2] and creep-fatigue interaction loading conditions;[11,12] and (6) establishing suitable methods for predicting LCF lives based on smooth specimen data.[12]
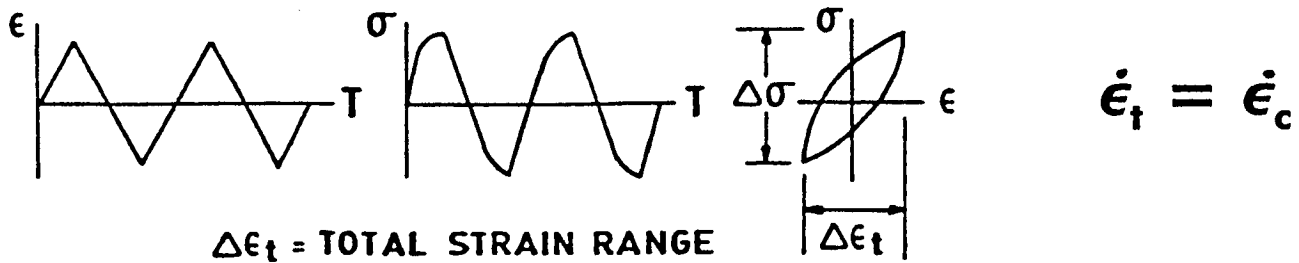
In the LCF tests conducted on alloy 800H employing either total or plastic strain as the control parameter, cyclic lives were found to be a strong function of temperature and strain rate. Under balanced cycle conditions (equal tension and compression loading rates in a cycle), in the temperature range between 600 °C to 900 °C, fatigue lives were dramatically reduced by both increasing temperature and decreasing strain rate.[1,2] Under balanced cycling conditions at 800 °C, a vacuum environment produced a nearly five-fold increase in life over that in air.[8] The shortened life in air was primarily attributed to oxidation-enhanced microcrack nucleation and microcrack growth.[3] At elevated temperatures, the loading waveform also had a large influence on fatigue life and crack growth rate. In tests on compact-tension specimens, in an air environment at 650 °C, an increase in crack growth rate has been observed when tensile hold times are included in the loading cycle.[10] The acceleration in cracking was associated with the occurrence of intergranular cracking that was attributed primarily to the introduction of creep mechanisms. On the other hand, in the LCF tests conducted at 850 °C on smooth specimens, the life under hold time conditions was seriously affected due to the combined influence of creep, fatigue, and oxidation.[12] The slow-fast loading has also greatly affected LCF lives both in air and vacuum compared to the corresponding symmetrical high strain rate tests at 800 °C.[6,8] The detrimental effect of slow-fast loading has been associated with the occurrence of extensive intergranular cavitation in the interior regions of the LCF specimens.[11]

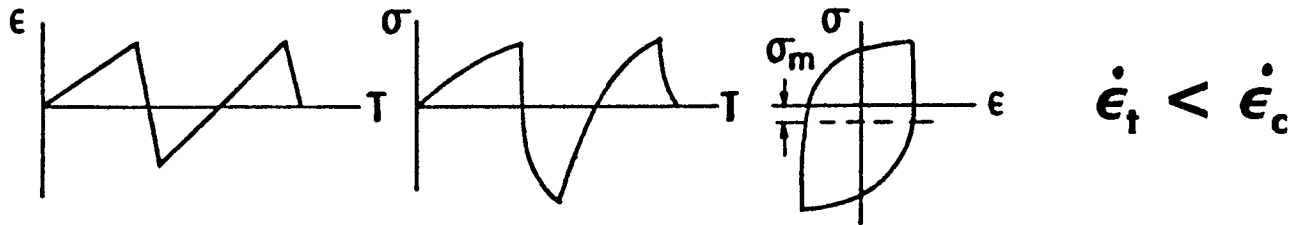Detailed investigations have been performed in the present study to characterize the phenomenological effects of
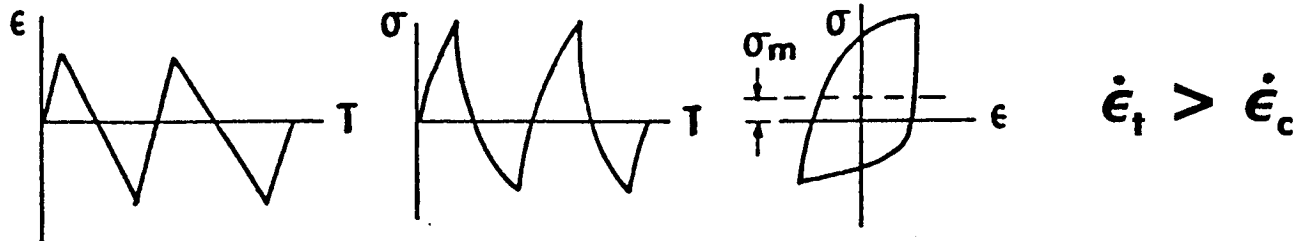
Fig. 1—(a) Waveforms employed in LCF testing; (b) schematic illustration of the stress response as a function of time; and (c) schematic representation of stress-strain hysteresis loops.

waveshape on LCF life and cyclic stress response behavior of alloy 800H at 850 °C. A detailed examination of the microstructural changes, deformation, crack initiation, and propagation modes has also been conducted with a view to understanding the damage modes which may govern the fatigue life under symmetrical (fast-fast (F-F) and slow-slow (S-S)) and asymmetrical (fast-slow (F-S) and slow-fast: (S-F)) loading conditions.

II. EXPERIMENTAL PROCEDURES

Alloy 800H, with the composition of (wt pct) 46.83Fe, 31.0Ni, 20.55Cr, 0.07Co, 0.17Mo, 0.25Al, 0.35Ti, 0.06C, 0.85Mn, and 0.32Si, was used in the form of 22-mm-diameter rods. The rods were solution annealed at 1175 °C for 1 hour followed by water quenching, which produced a grain size of ASTM 3. Parallel gage length cylindrical specimens with a gage diameter of 8 mm were then machined from the rods. The machined surfaces were polished in a direction perpendicular to the loading axis with emery papers of progressively increasing grit number from 320 to 600. The LCF tests were performed in air under fully reversed, axial strain control in a servohydraulic system of ± 100 kN dynamic load capacity. Axial strain was measured and controlled from a 25.4-mm gage length extensometer.

A nominal axial strain range of 0.6 pct and temperature of 850 °C was employed for all tests. Figure 1 depicts schematically the three types of loading waveforms that were

Table I. Influence of Waveform on LCF Life of Alloy 800H at 850 °C, $\Delta\varepsilon$ = 0.60 Pct

Waveform	ε_t, s^{-1}	ε_c, s^{-1}	Life, cycles
F-F	4×10^{-3}	4×10^{-3}	1930
S-S	4×10^{-5}	4×10^{-5}	1180
F-S	4×10^{-3}	4×10^{-5}	990
S-F	4×10^{-5}	4×10^{-3}	380

ε_t = tension going strain rate; and ε_c = compression going strain rate.

used. In the F-F (4×10^{-3} s^{-1}) and S-S (4×10^{-5} s^{-1}) tests, the tension and compression ramp rates are equal. In S-F cycling, the tension going strain rate (4×10^{-5} s^{-1}) is less than the compression going strain rate (4×10^{-3} s^{-1}), while in the F-S cycle, the tension going strain rate (4×10^{-3} s^{-1}) is higher than the compression going strain rate (4×10^{-5} s^{-1}). In general, a minimum of two specimens were tested for each loading condition. However, the results reported in this study are from single specimens tested under each loading condition. The cyclic stress response curves and fatigue life results from repeated tests are omitted here for brevity. The life corresponding to a 50 pct deviation from the plateau value of stress ratio ($\sigma_{min}/\sigma_{max}$) vs cycles curve was taken as the number of cycles to failure.

The specimens were inductively heated. Uniform heating of the specimen gage length was accomplished with the help of three separately adjustable sections of the induction
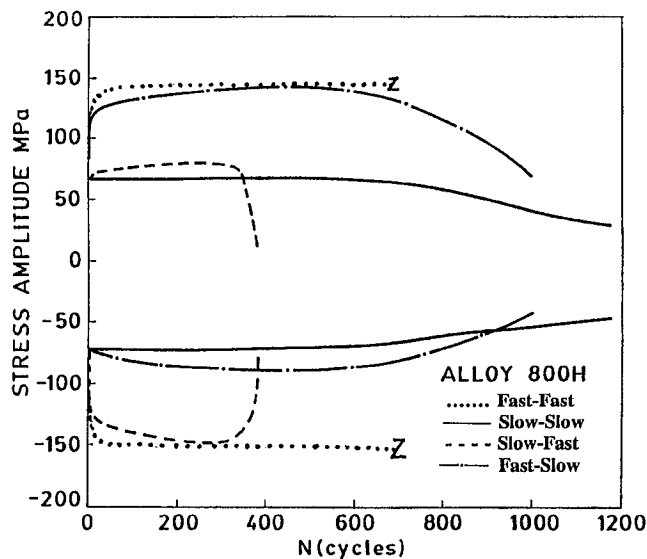
Fig. 2—Cyclic stress response as a function of waveform at 850 °C. Strain range: 0.60 pct.

coil and by carefully monitoring and controlling the specimen temperature using six thermocouples spot welded at equal intervals on the gage section. No cracks were found to initiate in the spot-welded regions during LCF testing. The temperature profile remained within ±2 °C of the nominal temperature throughout each test.

The fracture surfaces of fatigued samples were examined by optical microscopy and scanning electron microscopy (SEM) to determine the crack initiation and propagation modes. Studies were also conducted on longitudinal sections of failed specimens to document the behavior of surface cracks, interior damage, and microstructural changes that occurred during testing. Energy dispersive analysis of X-rays was conducted to identify various precipitates. The deformation substructure was studied by transmission electron microscopy (TEM). Samples for TEM examination were obtained from thin slices cut at a distance of 1 mm away from the fracture surface. The slices were mechanically thinned down to 250 μm and then electropolished in a solution containing 20 pct H_2SO_4 and 80 pct methanol, at 25 V and $\approx$0 °C, in a twin jet apparatus. Thin foils were examined in an electron microscope operating at an acceleration voltage of 200 keV. The orientation of TEM foil was normal to the loading axis.

III. RESULTS

A. Influence of Waveform on Fatigue Life and Cyclic Stress Response

The cyclic life as a function of waveform is shown in Table I. The greater endurance occurred for the balanced F-F test and the shortest life was shown by the unbalanced S-F test. The S-S and F-S tests have also revealed degrading effect on life but not as severe as that of the S-F test. The fatigue lives exhibited by different loading conditions are in the order: F-F > S-S > F-S > S-F. The influence of waveform on cyclic stress response is illustrated in Fig-

ure 2. The important points that emerge are as follows. (1) The cyclic stress response was strongly dependent on waveform. (2) The cyclic stress response was symmetrical in tension and compression for the balanced F-F and S-S tests. (3) Asymmetrical tests displayed unequal stress amplitudes in tension and compression; in F-S tests, the stress amplitude in tension was higher than in compression, and by contrast, in S-F tests, the stress amplitude in compression was higher than in tension. (4) The F-F and F-S tests exhibited a relatively short period of cyclic hardening followed by an extended period of a nearly saturation stress response. Toward the end of the tests, the tensile stress amplitude decreased rapidly, indicating the formation of microcracks and their subsequent growth. (5) The S-S tests exhibited a stable stress response from the very beginning. (6) In S-F condition, there was a negligible amount of cyclic strain hardening in tension, although the compressive half clearly revealed a prolonged stage of cyclic hardening. (7) In the F-S test compared to the F-F test, the cyclic deformation in the compression half, in the early hardening and saturation stages, took place at much lower stresses.

The half-life hysteresis loops of F-S and S-F tests (Figure 3) show large amounts of tensile and compressive mean stresses, respectively. In the F-F and S-S tests, the tension and compression halves of the hysteresis loops were symmetrical and did not develop any mean stress. The inelastic strains attributed to creep ($\Delta\varepsilon_{IN-C}$) and pure plasticity ($\Delta\varepsilon_{IN-P}$) during one cycle of different loading conditions at half-life were investigated using the concepts of Strainrange Partitioning.[13,14,15] The partitioning of total inelastic strain into pure plasticity and creep was based on the flow response of the material in the tension and compression portions of the cycle. The detailed procedure of computation is outlined in Reference 15. The inelastic strain in the F-F test is considered to be time independent and therefore purely plastic. The computed results indicate that more inelastic deformation is encountered in the S-S test as compared with F-S and S-F tests (Table II).

B. Fractographic Observations, Deformation, and Precipitation Behavior

In F-F tests, the crack initiation and propagation occurred in a classical transgranular fatigue fracture mode (Figures 4(a) (b)). The smaller strain rate S-S tests and unbalanced S-F tests exhibited intergranular fracture (Figure 5(a)). In F-S tests, the fracture was similar to a tensile fracture accompanied by necking (Figure 5(b)). There has been significant departure in the original geometry of the specimen in S-F and F-S tests. The S-F induced geometrical instability in the form of slight bulging, while in the F-S test, the instability was manifested in the form of necking. Similar types of instabilities have been reported earlier for alloy 800 H in hold time tests conducted at 850 °C.[15]

The cyclic deformation in all loading conditions led to the formation of well-defined subgrains with regularly arranged dislocations in the subgrain walls. For F-F conditions, the subgrain interiors contained considerable randomly oriented dislocations (Figure 6). Multiple slip in some of the grains was also observed, suggesting that the mode of deformation was predominantly homogeneous at 850 °C. Although the starting material was free from precipitates other than primary Ti(CN), material in all the test-

ing conditions showed substantial amounts of intra- and intergranular precipitation. Figure 7 illustrates the morphology and distribution of precipitates in different tests. In all the loading conditions, the intergranular precipitates were generally rather coarse compared to intragranular precipitates and mainly consisted of chromium-rich $M_{23}C_6$ and TiC. The proportion of $M_{23}C_6$ was much larger on the grain boundaries compared to TiC in all the tests. The density of intragranular precipitates was comparatively less after F-F testing and more after S-S testing. Apart from these discrete carbides, marked precipitation of $M_{23}C_6$ particles in the

form of parallel plates occurred at grain and incoherent twin boundaries (Figure 8) in F-F, F-S, and S-F tests. This type of precipitation was scarcely found after S-S testing.

IV. DISCUSSION

A. Damage Processes under Balanced Cycle Conditions

Based on the results in Section III, deductions can be inferred about the time-dependent mechanisms controlling cyclic life under different loading conditions. In the F-F
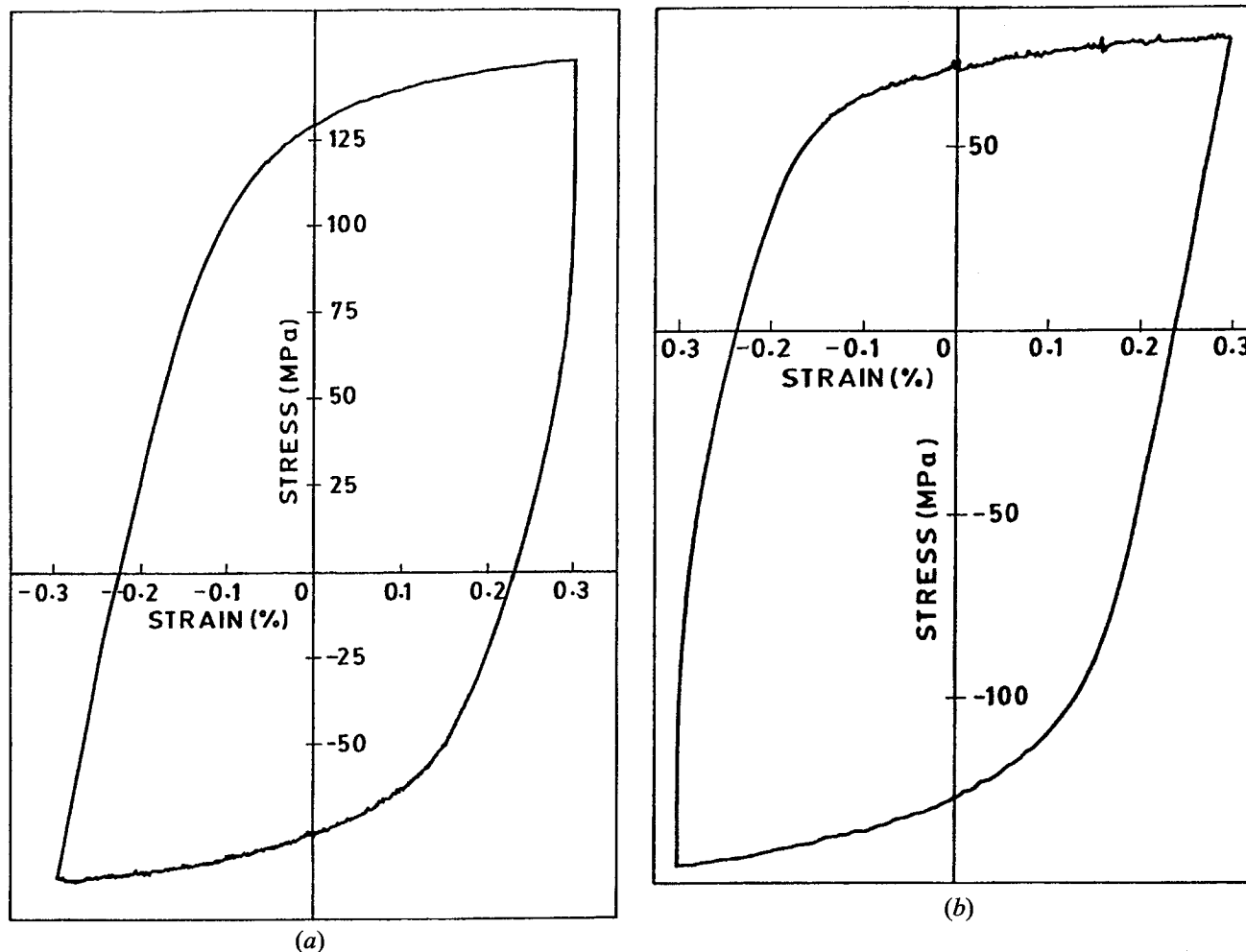

Fig. 3—Half-life hysteresis loop in (a) F-S and (b) S-F tests.

Table II.   Values of Elastic, Plastic, and Creep Strains as a Function of Waveform

Waveform	Strain Range, Pct						
	$\Delta \varepsilon_t$	$\Delta \varepsilon_e$	$\Delta \varepsilon_{in}$	$\Delta \varepsilon_{pp}$	$\Delta \varepsilon_{cp}$	$\Delta \varepsilon_{pc}$	$\Delta \varepsilon_{cc}$
F–F	0.600	0.195	0.405	0.405	—	—	—
S–S	0.600	0.105	0.495	0.033	—	—	0.462
F–S	0.600	0.145	0.455	0.124	—	0.381	—
S–F	0.600	0.127	0.473	0.072	0.401	—	—

$\Delta \varepsilon_t$ = total axial strain range; $\Delta \varepsilon_e$ = elastic strain range; and $\Delta \varepsilon_{in}$ = inelastic strain range.
$\Delta \varepsilon_{pp}$ = tensile plastic strain reversed by compressive plastic strain.
$\Delta \varepsilon_{cp}$ = tensile creep strain reversed by compressive plastic strain.
$\Delta \varepsilon_{pc}$ = tensile plastic strain reversed by compressive creep strain.
$\Delta \varepsilon_{cc}$ = tensile creep strain reversed by compressive creep strain.
$\Delta \varepsilon_{in}$ is partitioned into $\Delta \varepsilon_{pp}$, $\Delta \varepsilon_{cp}$, $\Delta \varepsilon_{pc}$, and $\Delta \varepsilon_{cc}$ components using the Strain Range Partitioning procedure outlined in Ref. 15.
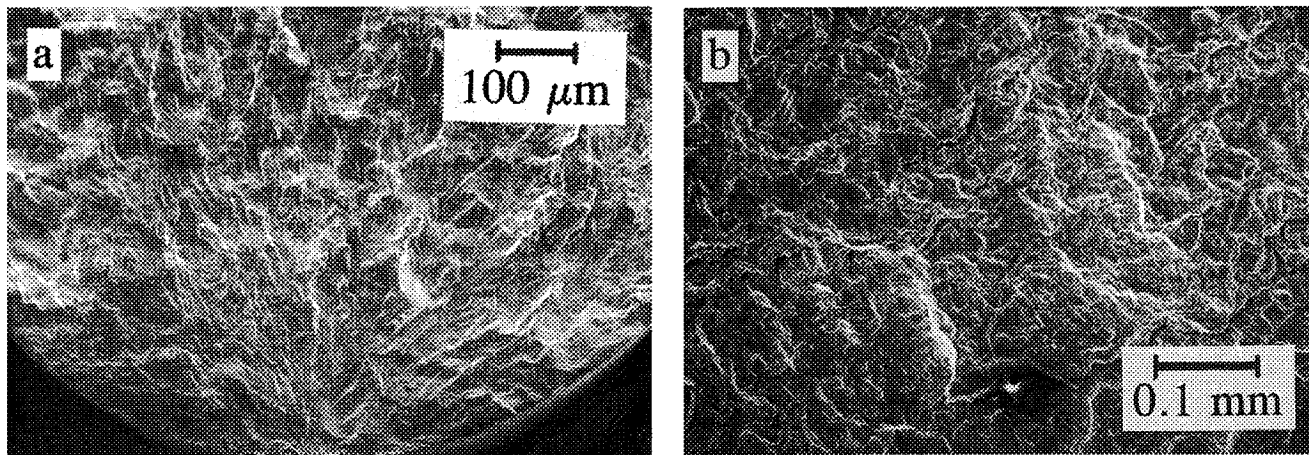
Fig. 4—SEM photographs illustrating (a) transgranular crack initiation and (b) transgranular propagation in an F-F test at 850 °C.
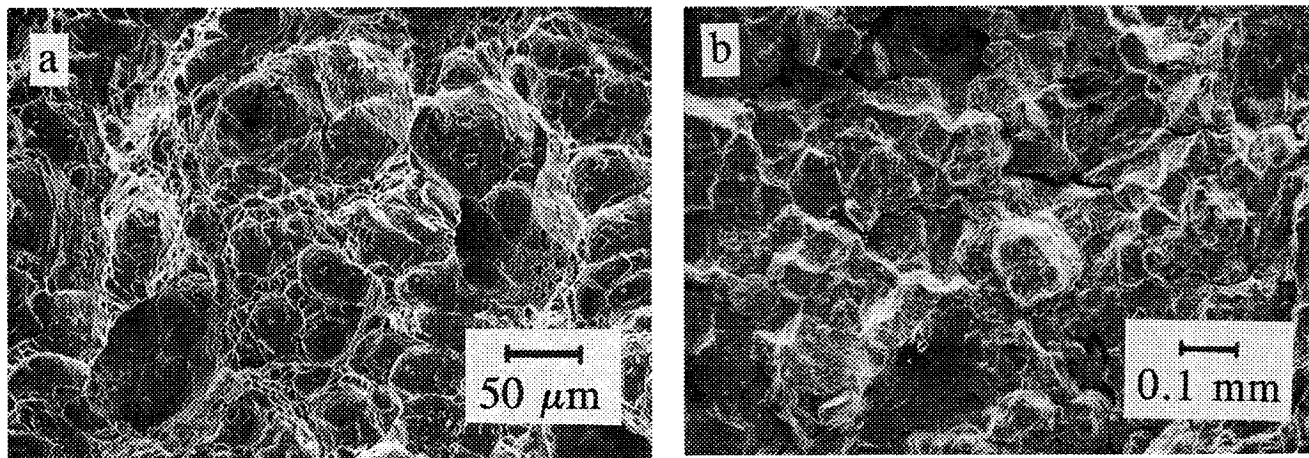

Fig. 5—SEM photographs showing (a) dimples characteristic of ductile failure in an F-S test and (b) intergranular failure in a S-F test.

test, oxidation, dynamic strain aging, and massive precipitation of $M_{23}C_6$ were noticed to operate concurrently. The information obtained on microcracks of the longitudinal sections (Figure 9) in conjunction with observations made on the fracture surfaces (Figure 4(a)) reveals that the crack initiation and propagation in the F-F tests occurred in a direction normal to the applied stress axis by transgranular stage-II mechanisms. The F-F cycling caused the spallation of surface oxide scales and led to the development of a very rough surface. The microcracks generally displayed a thin oxide layer on the crack flanks and a pronounced tendency for branching. In F-F tests, the transgranular crack initiation by crystallographic slip is bypassed and the initiation took place by stage-II mechanisms. The thin adherent oxide layer that formed during the heating and equilibration period prior to the commencement of testing seems to prevent the development of active slip bands in surface grains that normally are responsible for stage-I cracking. Within just a few cycles, surface oxide cracks, under the action of mechanical strain, lead to stage-II crack initiation. In F-F tests, the oxidized appearance of crack tips suggests the continuing involvement of oxidation even in the crack growth stage. A comparative evaluation of the transgranular cracking behavior of alloy 800H has been made by Bressers et al.[3] in air and vacuum over a range of strain rates at 800 °C. The results indicated that,
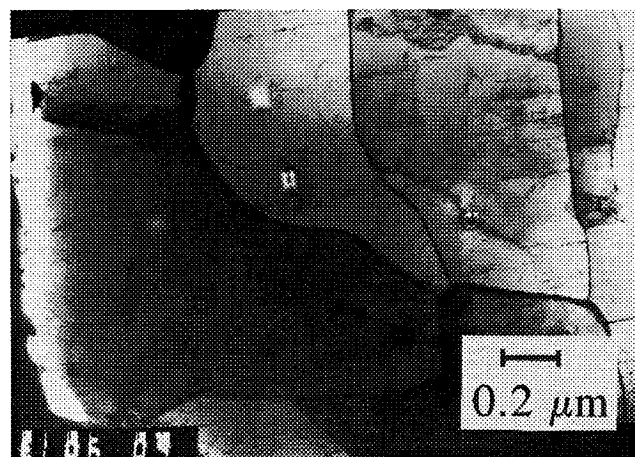

Fig. 6—TEM photograph depicting the substructure in the fast-fast test; the photograph shows well-developed subgrain walls and randomly distributed dislocations in the interior regions of the subgrains.

besides the enhancement of crack nucleation, oxidation also accelerates the growth rate of microcracks by enhancing the growth rate of individual cracks as well as through multiple crack coalescence. Oxide-enhanced transgranular crack growth has been suggested to occur as a result of the repeated formation of an oxide layer at the crack tip, its rup-
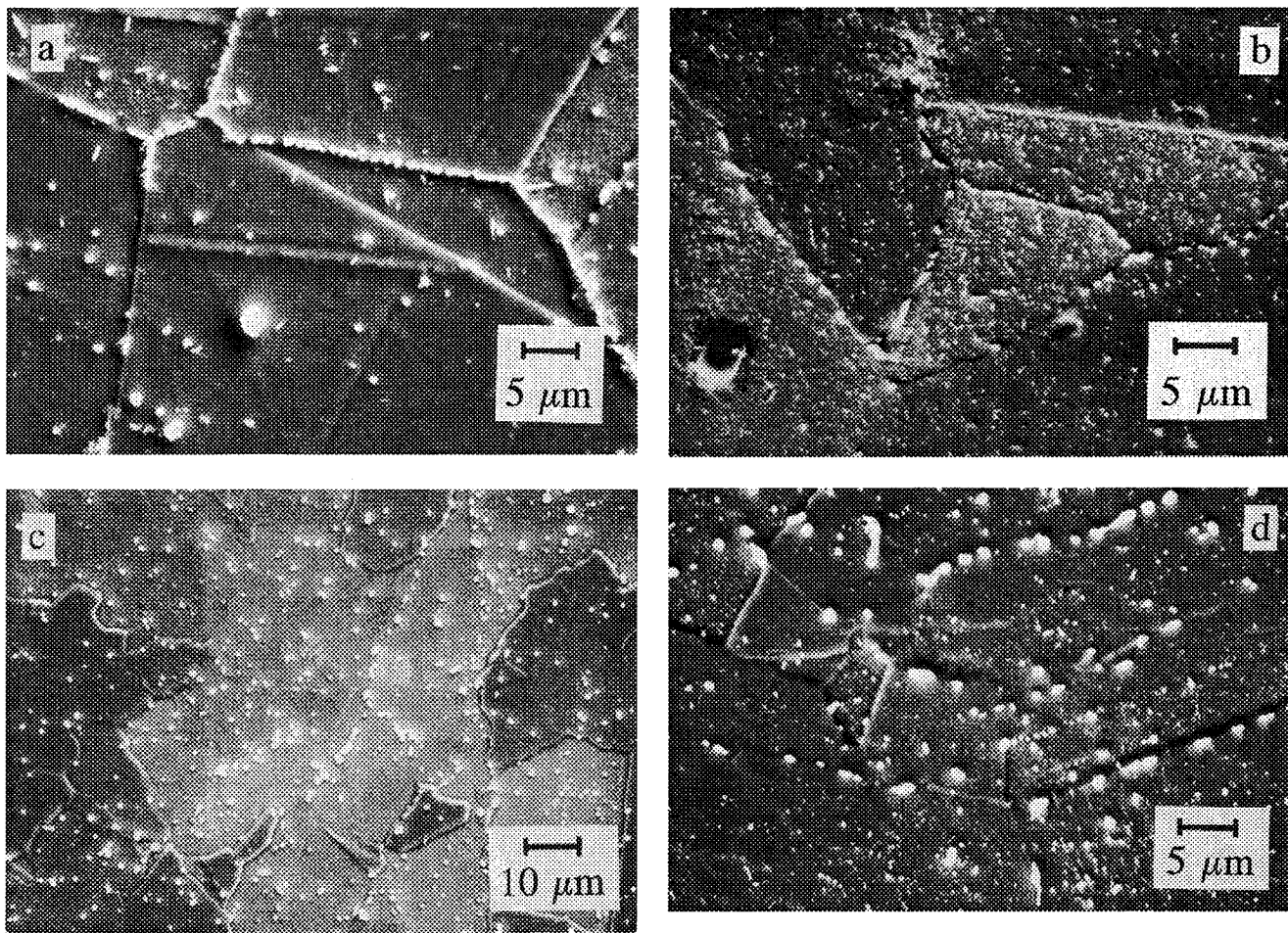
Fig. 7—SEM photographs illustrating the type, size, and distribution of intra- and intergranular precipitates in (a) F-F, (b) S-S, (c) F-S, and (d) S-F tests.

ture, and the exposing of fresh metallic material to the environment in each cycle.[17] Oxidation at the crack tip would render a thin layer of material more brittle and so would assist crack propagation.[18]

In F-F tests, the plastic regions of stress-strain hysteresis loops displayed serrated flow (Figure 10). Serrated flow appears as a consequence of dynamic strain aging (DSA) of mobile dislocations. Recent studies on austenitic stainless steels and NIMONIC* PE 16 superalloy have clearly dem-

*NIMONIC is a trademark of INCO Alloys International, Inc., Huntington, WV.

onstrated the detrimental effects of DSA on strain-controlled fatigue life.[18,19,20] Dynamic strain aging has been noted to cause the shortening of the crack initiation phase in alloy 800H in the tests performed in vacuum at 600 °C.[21] Under the influence of DSA, the higher response stresses developed during cyclic deformation could lead to a large stress concentration at the crack tip and would enhance the crack growth rate.

The massive precipitates of $M_{23}C_6$ in the form of parallel plates occurred very prominently in F-F tests compared to the conditions that contained the fast deformation rate in only one leg of the loading. This type of precipitation showed a stronger preference to form on those grains and incoherent twin boundaries which are beneath the fracture surface (Figure 8) or in the areas surrounding the macro-
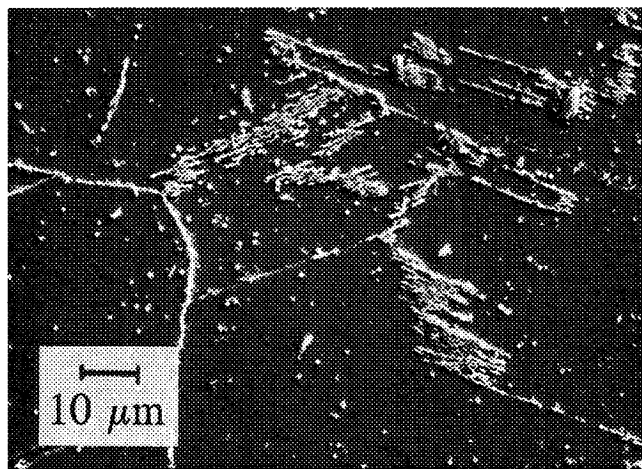

Fig. 8—SEM photographs illustrating the massive precipitation of $M_{23}C_6$ on the incoherent twin boundaries in an F-F test in the region beneath the fracture surface.

cracks away from the fracture zone (Figure 9). Massive precipitates were not found in the near-surface regions, as demonstrated clearly in Figure 8. Supersaturation of carbon is a necessary prerequisite for the occurrence of massive precipitates.[2] The depletion of substantial amounts of chromium due to formation of surface oxide scales and simultaneous decarburization could be expected to reduce the
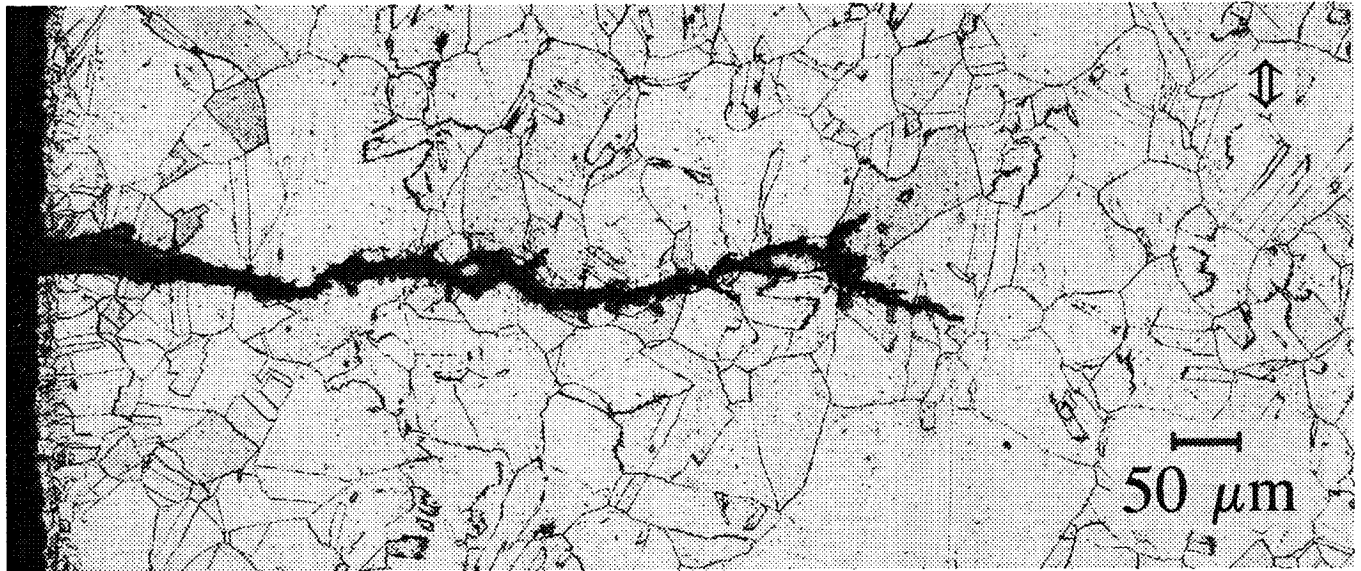
Fig. 9—Secondary crack in an F-F test, illustrating the crack initiation and propagation by transgranular stage-II mechanism. The arrows indicate the direction of applied stress.
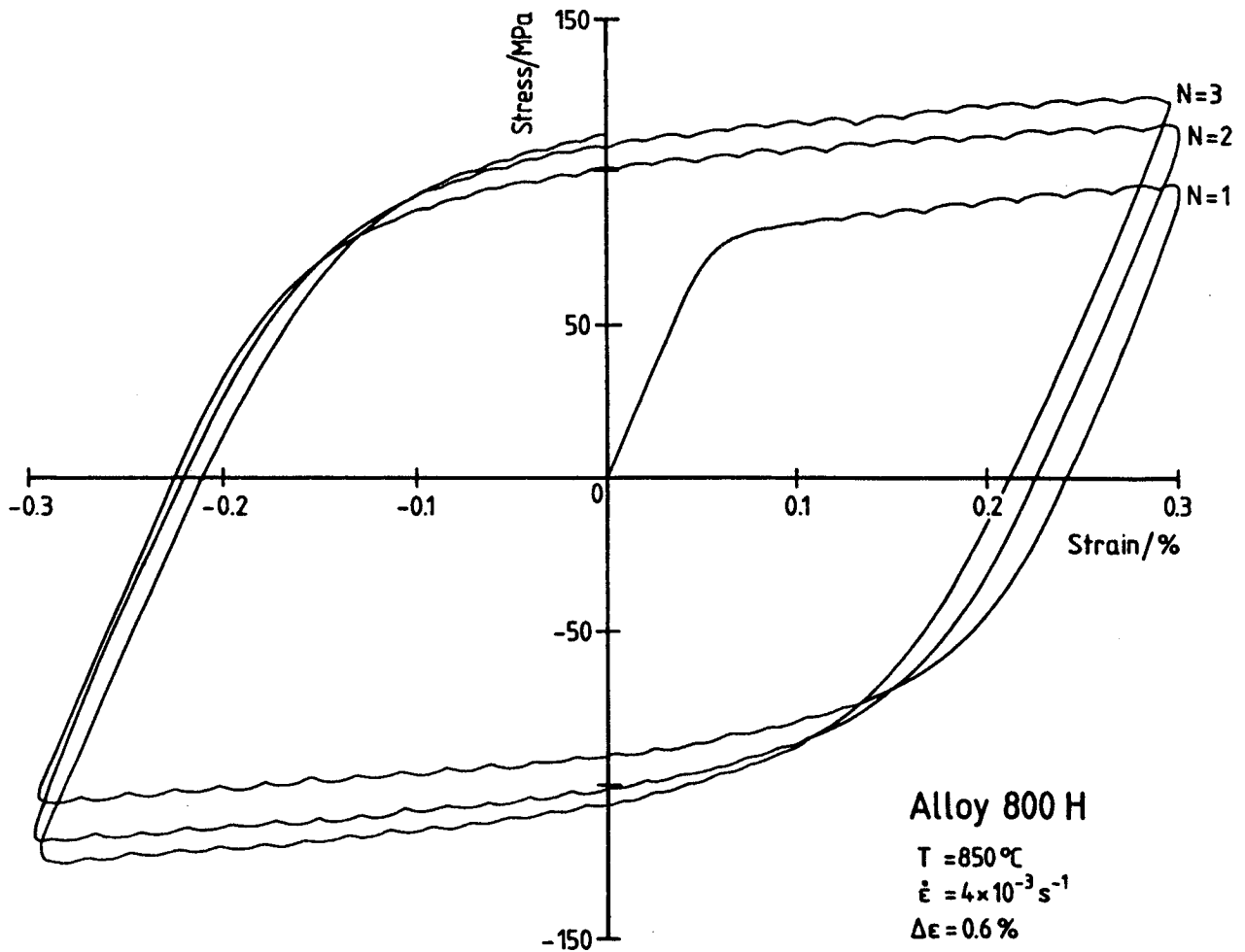

Fig. 10—Stress-strain hysteresis loops depicting serrated flow in an F-F test.

potential for the formation of massive precipitates in the near-surface regions. The presence of such precipitates may lead to local regions of differential strength and ductility.

The concentration of deformation in the regions of low strength and high ductility facilitate rapid initiation and propagation of cracks. The massive precipitation in the bulk
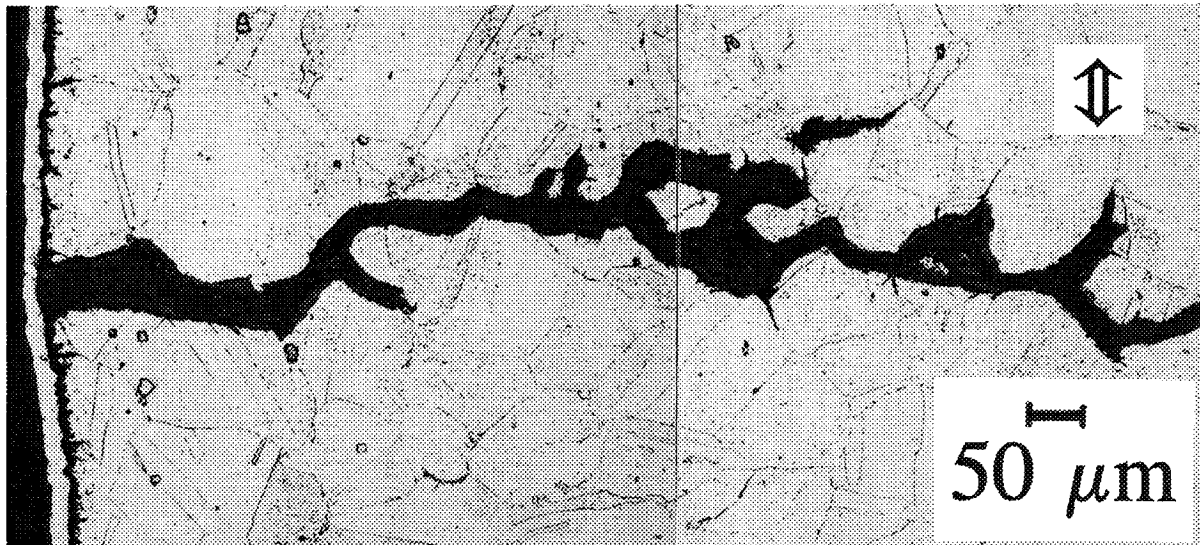
Fig. 11—Optical micrograph of a secondary crack illustrating the oxidation assisted intergranular crack initiation and propagation in a S-S test. The arrows indicate the direction of applied stress.

renders the alloy susceptible to intergranular corrosion in air due to a sharp decline in chromium concentrations in the regions adjoining the lamellae. It is to be expected that the life in F-F tests would be longer without the interference of the aforementioned time-dependent mechanisms.

It was clear from Table I that decreasing the ramp rate from 4×10^{-3} s^{-1} (F-F) to 4×10^{-5} s^{-1} (S-S) in a balanced cycle reduces the fatigue life. Three important changes were found to be associated with this reduction: there is a decrease in stress amplitude (Figure 2); an increase in the effective inelastic strain range (i.e., an increase in the width of the hysteresis loop at zero stress, Table I); and visible changes in crack initiation and propagation modes from transgranular in the F-F to purely intergranular in the S-S test. The intergranular cracking in the S-S test resulted from the damaging effects of oxidation, and there has been no outward appearance of creep damage either in the form of triple-point wedge cracking or r-type cavities. In several studies,[22,23,24] it has been noticed that the balanced cycle conditions are not the most conducive for development of creep damage in the form of intergranular cavities and wedge cracking. In the S-S tests, the tensile and compressive rates are equal. Any bulk cavity damage produced in the tensile going direction is equal to the damage recovered in the compressive going direction, and therefore, it is to be expected that there would be little, if any, net accumulation of creep damage. Sidey and Coffin[22] and Min and Raj[23] have shown that creep cavitation is reversible upon reversal of loading from tension to compression for small cavity sizes. This type of reversal occurs as a result of sintering of sufficiently small cavities during the compression part of the cycle.[24] Balancing of tensile creep damage with compressive creep damage would be expected, according to the tenants of Strainrange Partitioning,[14] to result in longer cyclic lives compared to unbalanced cyclic tensile creep damage.

Many of the cracks in S-S tests were initiated by the rupture of oxide scales formed at the surface-connected grain boundaries. Once the crack was initiated at the surface, further diffusion of oxygen and extended grain bound-
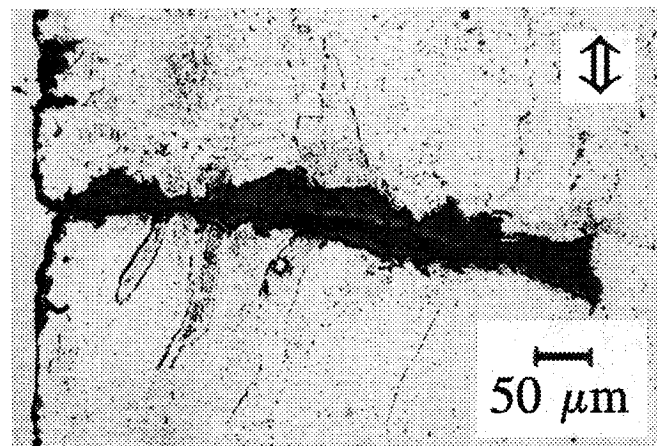

Fig. 12—Oxidation assisted transgranular crack initiation and propagation in an F-S test. The arrows indicate the applied stress direction.

ary oxidation ahead of the crack weakened the boundary and promoted intergranular crack propagation, as shown in Figure 11. The oxidation effects were enhanced by lowering the strain rate, allowing more oxidation at the crack tips and surface. These observations suggest that the life in an S-S test is governed by the combined influence of oxidation and by the increase in inelastic strain component over that observed in F-F tests (Table II).

B. Damage Modes under Asymmetrical Conditions

The capacity of a material to develop and sustain mean stress under strain-controlled conditions depends upon several factors: the temperature in the tensile and compressive ends of the strain cycle, the straining rates in each direction of loading, and the ratio of the inelastic to elastic strain range of the cycle.[25] The F-S and S-F waveforms imposed isothermally on the alloy 800H samples introduced considerable amounts of tensile and compressive mean stresses, respectively. The damaging nature of mean stresses developed in this manner is addressed in Reference 25. For pur-
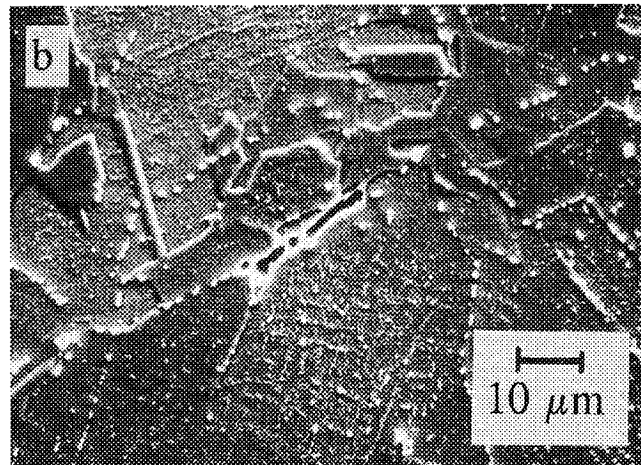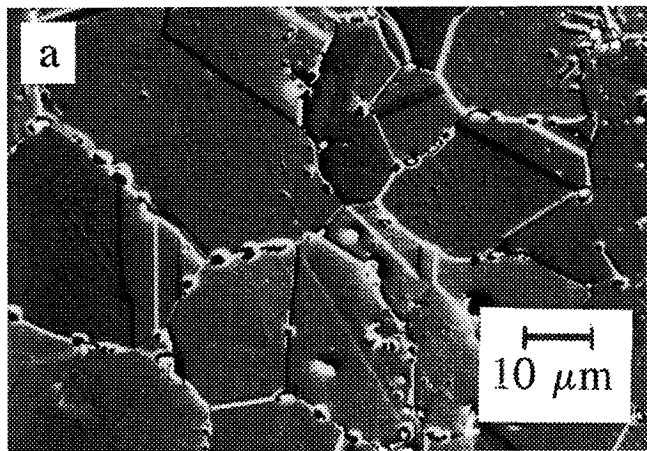
Fig. 13—SEM photographs showing intergranular creep cavity damage in the bulk of the specimen in a S-F test: (a) cavities associated with grain boundary particles in the region beneath the fracture surface and (b) interlinkage of cavities resulting in a crack in a region remote from the fracture surface.

poses herein, the damaging aspects of mean stresses are not addressed directly but rather are considered to be accounted for inherently in the Strainrange Partitioning method for damage assessment and life prediction.

The specimens in F-S and S-F tests experienced internal deformation ratcheting in each cycle. Since deformation rates in the tension going direction are different from those in the compression going direction in F-S and S-F tests, plastic deformation in tension and creep in compression were accumulated, respectively, under F-S cycling, whereas under S-F loading, creep in tension and plastic deformation in compression were accumulated, respectively. The deformation ratcheting of both plasticity in one direction and creep in another constitutes a serious damaging mode in the asymmetrical tests. For F-S conditions, the fracture occurred by tensile necking instability (Figure 4(d)). The accumulation of microscopic inelastic tensile strain, which is not recovered during the compressive portion of the cycle, would contribute to this phenomenon. The strains can become concentrated in the regions of initial plasticity, and this detrimental effect is additional to other time-dependent effects.

As for F-F conditions, the crack initiation and propagation occurred by a transgranular stage-II mechanism in F-S tests (Figure 12). The oxidation of surface and crack flanks was much more severe in the F-S test than the F-F test. This has occurred because of the special opportunity provided for a thick adherent oxide to develop during the slow compression going ramp. Considering that the time for one cycle in an F-S test is smaller than in an S-S test, it would be expected that environmental damage would be smaller in the F-S test. Still, F-S loading was found much more damaging than S-S loading because of the shape instability resulting from the deformation ratcheting effects. The predominance of necking instability in the later stages of F-S tests speeds up failure as is manifested by the rapid drop in cyclic stress response. No creep damage was seen in F-S tests.

For S-F conditions, the inclusion of slow tensile strain rate into the fatigue cycle enabled creep cavitation damage to accumulate at grain boundary particles in the bulk. The creep damage produced during the tensile going strain rate was not sintered by rapid compressive straining. Therefore,
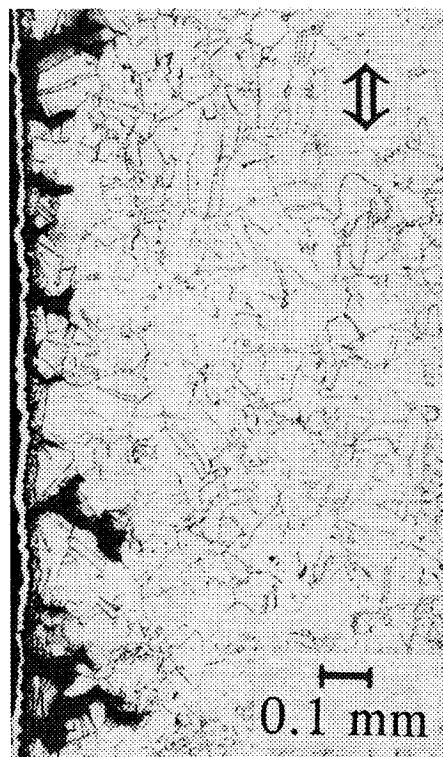

Fig. 14—Optical micrograph of a longitudinal section showing multiple intergranular cracks on the surface of a specimen subjected to S-F cycling. The arrows indicate the applied stress direction.

a net buildup of intergranular cavity damage took place, especially in the regions close to the fracture surface, and the failure resulted by an intergranular crack growth mode. Figure 13(a) clearly illustrates the development of intergranular cavities (R type) associated with grain boundary precipitates adjacent to the fracture surface, while Figure 13(b) shows cavity formation and linkage on grain boundaries in the regions remote from the fracture surface. In addition to bulk intergranular damage, a large number of surface intergranular cracks (Figure 14) had initiated and grown to depths of about 1 mm. Presumably, these had ceased growing when the propagation of cracks lying in the
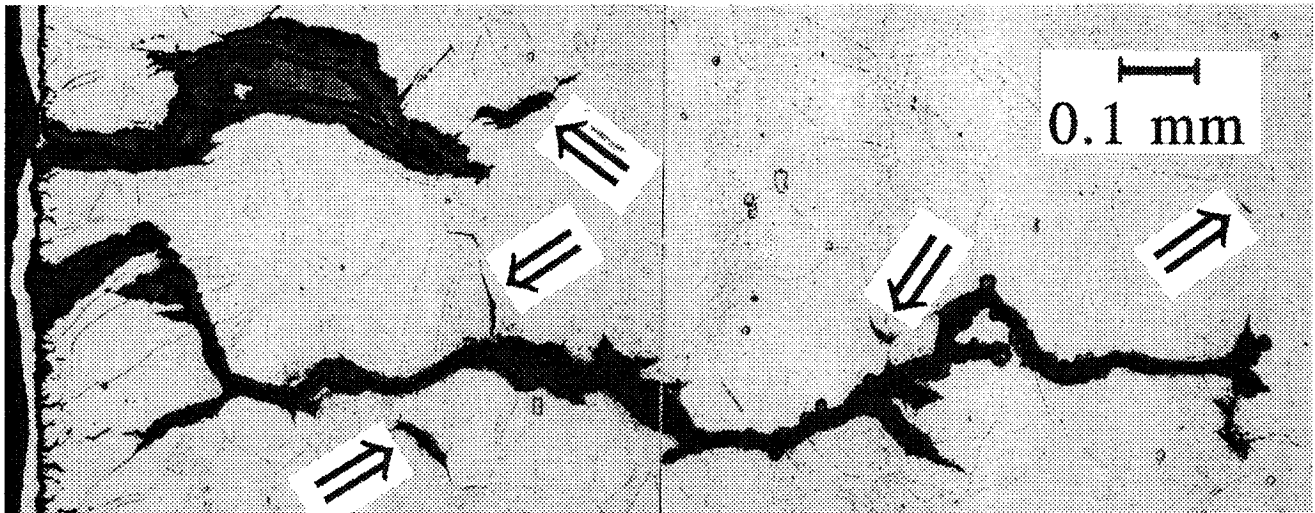
Fig. 15—Optical micrograph illustrating intergranular crack propagation in the S-F test. Crack flanks contain thick layers of oxide. Creep cracks are indicated by arrows.

vicinity of the fracture zone became dominant (Figure 15). Near the surface, the environmental damage effects are severe and the diffusion of environmental species down the grain boundaries can cause a reduction in the boundary cohesive strength. This effect may enhance sliding in the contaminated grain boundary and hence promote subsequent cracking, as shown in Figure 14. Direct crack initiation of the oxidized and embrittled grain boundaries may be an alternative mode of fracturing. Whatever the mechanism of crack initiation might be, oxidation appears to affect primarily the initiation and the near-threshold crack growth stages in S-F tests. Fatigue crack growth behavior of type 304 stainless steel, when one S-F cycle was interspersed between the F-F cycles, was investigated at 873 K by Okazami et al.[27] It was noted that the fatigue crack growth rate in the F-F cycles is accelerated by the introduction of one S-F cycle. A longitudinal section through the specimen at the region where one S-F cycle was introduced showed wedge-type cracks at the grain boundaries. This observation clearly indicates that the introduction of S-F cycling produces a creep-effect zone and accelerates the crack growth until the crack escapes from the creep-effected zone. Thus, for S-F conditions, creep cavitation and oxidation damage both contribute to lower fatigue life. The damage modes governing the fatigue life of alloy 800H as a function of waveshape are summarized in Table III.

V. SUMMARY

1. Fatigue life of alloy 800H is strongly dependent on waveshape. Life exhibited by different waveforms are in the following order: F-F > S-S > F-S > S-F.
2. Cyclic stress response varied as a complex function of waveshape. Symmetrical F-F and S-S tests displayed equal stress amplitudes in tension and compression, whereas unbalanced F-S and S-F tests showed asymmetrical stresses. The F-F and F-S waveforms promoted cyclic hardening in the initial stages followed by a nearly stable stress response, while S-S and S-F tests exhibited stable tensile stress response from the beginning.

Table III. Summary of Waveform Effects

Waveform	Crack Initiation and Propagation	Damage Modes
F-F	transgranular	F + MP + DSA + O
F-S	transgranular	F + O + DR + MP
S-S	intergranular	F + O + IS
S-F	intergranular	F + O + C + MP

F = fatigue; MP = massive precipitation; O = oxidation; DR = deformation ratcheting; IS = inelastic strain; and C = creep damage.

3. The fracture modes depended on the tension going deformation rate. The fast deformation rate during tension going led to transgranular crack initiation and propagation, while slow ramping caused intergranular initiation and propagation.
4. Ramping at different rates in tension and compression created deformation ratcheting in F-S and S-F tests and influenced the failure modes to a greater extent.
5. Cyclic life was influenced by synergistic interactions between a number of time-dependent mechanisms. Dynamic strain aging, massive precipitation of $M_{23}C_6$, and oxidation were found to coexist in F-F tests. In S-S tests, the life was affected by time-dependent deformation and oxidation. Oxidation and deformation ratcheting were the principal mechanisms operating under F-S conditions. Synergistic interactions occurred in S-F tests between damage due to fatigue, creep cavitation, and oxidation.

REFERENCES

1. J. Bressers, U. Schusser, W. Weise, R. De Cat, and E. Fenske: Cost 501 Final Report, EUR 11693 EN (1988), Commission of the European Communities, 1988, pp. 1-56.
2. K. Bhanu Sankara Rao, H. Schiffers, H. Schuster, and H. Nickel: Metall. Mater. Trans. A, 1996, vol. 27A, pp. 255-68.
3. J. Bressers, U. Schusser, and B. Ilschener: in Low Cycle Fatigue and Elasto-Plastic Behavior of Materials, K.T. Rie, ed., Elsevier Applied Science, London, 1987, pp. 365-70.
4. J. Barbehon, A. Rahmel, and M. Schutze: in Low Cycle Fatigue and

Elasto-Plastic Behavior of Materials, K.T. Rie, ed., Elsevier Applied Science, London, 1987, pp. 371-77.

5. B.A. Lerch, B. Kempf, D. Steiner, and V. Gerold: *Proc. 7th Int. Conf. on the Strength of Metals and Alloys*, Montreal, H.J. McQueen, J.-P. Bailon, J.I. Dixon, J.J. Jonas, and M.G. Akbon, ed. Pergamon Press, Oxford, 1986, pp. 1299-1304.

6. B. Kempf, K. Bothe, and V. Gerold: Paper presented at *6th Eur. Conf. on Fracture*, Amsterdam, 1986.

7. K. Bothe, B. Kempf, and V. Gerold: in *High Temperature Alloys for Gas Turbines and other Applications*, W. Betz, R. Brunetaud, D. Coutsouradis, H. Fischmeister, T.B. Gibbons, I. Kvernes, Y. Lindblom, J.B. Marriott, and D.B. Meadowcroft, eds., D. Reidel Publishing Company, Dordrecht, 1986, pp. 1517-26.

8. B. Kempf, K. Bothe, and V. Gerold: *Z. Metallkd.*, 1986, vol. 77, pp. 576-81.

9. J. Bressers, W. Weise, and T. Hollstein: in *Low Cycle Fatigue and Elasto-Plastic Behavior of Materials*, K.T. Rie, ed., Elsevier Applied Science, London, 1987, pp. 655-60.

10. K.Y. Hour and J.F. Stubbins: *Metall. Trans. A*, 1989, vol. 20A, pp. 1727-34.

11. B. Kempf, K. Bothe, and V. Gerold: in *Low Cycle Fatigue and Elasto-Plastic Behavior of Materials*, K.T. Rie, ed., Elsevier Applied Science, London, 1987, pp. 271-76.

12. P. Agatonovic and N. Taylor: in *Proc. 6th Int. Conf. on Mechanical Behavior of Materials—VI*, Kyoto, Japan, M. Jono and T. Inoue, eds., Pergamon Press, Oxford, 1992, pp. 303-10.

13. G.R. Halford, M.H. Hirschberg, and S.S. Manson: *Temperature Effect on the Strainrange Partitioning Approach for Creep-Fatigue Analysis*, ASTM STP 520, ASTM, Philadelphia, PA, 1973, pp. 658-69.

14. S.S. Manson: *The Challenge to Unify Treatment of High Temperature Fatigue—A Partisan Approach Based on Strain Range Partitioning*, ASTM STP 520, ASTM, Philadelphia, PA, 1973, pp. 744-82.

15. S.S. Manson, G.R. Halford, and A.J. Nachtigall: *Advances in Design for Elevated Temperature Environment*, ASME, Fairfield, NJ, 1975, pp. 17-28.

16. H.P. Meurer, G.H.K. Gnirss, W. Mergler, G. Raule, H. Schuster, and G. Ulrich: *Nucl. Technol.*, 1984, vol. 66, pp. 315-23.

17. L.F. Coffin, Jr.: *Metall. Trans.*, 1974, vol. 5, pp. 1053-64.

18. K. Bhanu Sankara Rao, M. Valsan, R. Sandhya, S.L. Mannan, and P. Rodriguez: *Trans. Ind. Inst. Met.*, 1991, vol. 44, pp. 255-71.

19. K. Bhanu Sankara Rao, M. Valsan, R. Sandhya, S.L. Mannan, and P. Rodriguez: *High Temp. Mater. Processes*, 1986, vol. 7, pp. 171-78.

20. M. Valsan, K. Bhanu Sankara Rao, D.H. Shastry, and S.L. Mannan: *Metall. Mater. Trans. A*, 1994, vol. 25A, pp. 159-71.

21. J. Bressers, L. Remy, and W. Hoffelner: *Proc. Conf. High Temperature Alloys for Gas Turbines and Other Applications*, Leigh, Oct. 6–9, 1986, W. Betz, R. Brunetaud, D. Coutsouradis, H. Fischmeister, T.B. Gibbons, I. Kvernes, Y. Lindblom, J.B. Marriott, and D.B. Meadowcroft, eds., D. Riedel Publishing Company, Dordrecht, 1986, p. 441.

22. D. Sidey and L.F. Coffin, Jr.: *Low Cycle Fatigue Damage Mechanisms at High Temperature*, ASTM STP 675, ASTM, Philadelphia, PA, 1979, pp. 528-68.

23. B.K. Min and R. Raj: *A Mechanism of Intergranular Fracture during High Temperature Fatigue*, ASTM STP 675, ASTM, Philadelphia, PA, 1979, pp. 569-91.

24. S.S. Manson and G.R. Halford: *Isr. J. Technol.*, 1993, vol. 21, pp. 29-53.

25. G.R. Halford and A.J. Nachtigall: *J. Aircraft*, 1980, vol. 17, pp. 598-604.

26. D.C. Lord and L.F. Coffin, Jr.: *Metall Trans.*, 1973, vol. 4, pp. 1647-53.

27. M. Okazami, I. Hotari, and T. Koizumi: *Metall. Trans. A.*, 1984, vol. 15A, pp. 1731-39.